RESEARCH PAPER

Oil-Pressure Based Apparatus for *In-Situ* High-Energy Synchrotron X-Ray Diffraction Studies During Biaxial Deformation

R.R. Kamath[1] · J. Thomas[1] · A.C. Chuang[2] · B. Barua[1] · J.-S. Park[2] · L. Xiong[1] · T.R. Watkins[3] · S.S. Babu[4] · G. Cola[5] · D. Singh[1]

Abstract

Background Understanding biaxial loading response at the microstructural level is crucial in helping better design sheet manufacturing processes and calibrate/validate material deformation models.

Objective The objective of this work was to develop a low-cost testing apparatus to probe, with sufficient spatial resolution, the micro-mechanical response of a sheet material *in-situ* under biaxial loading conditions.

Methods The testing apparatus fabricated as a part of this study operates in a similar fashion to a standard bulge test and uses oil pressure to generate biaxial loading conditions. This biaxial testing apparatus was operated within a synchrotron beamline to characterize the mechanical response of a flash-processed steel sheet using *in-situ* high-energy X-ray diffraction (XRD) measurements. The GSAS-II package was utilized to develop a workflow for the analysis of the large volume of diffraction data acquired. The workflow was then used to extract the peak position, width, and integrated intensity of the XRD peaks corresponding to the major body-centered cubic phase.

Results The equi-biaxial nature of the loading in the measured area was independently corroborated using experimental (XRD) and simulation (finite element analysis) methods. Furthermore, we discuss the evolution of elastic strain in the major body-centered cubic phase as a function of applied oil pressure and location on the steel sheet.

Conclusions A key advantage of the biaxial apparatus fabricated in this synchrotron study is demonstrated using the results obtained for the flash-processed steel sheet – i.e., mapping the lattice plane-dependent response to biaxial loading for a relatively large sample area in a spatially resolved manner.

Keywords *In-situ* synchrotron diffraction · Biaxial loading · Flash-processed steel · Elastic strain · Finite element simulations

Introduction

Sheet metal forming plays an integral part in the production of lightweight structures in the automotive and aerospace industries [1–3]. This operation predominantly subjects the sheet metal to a biaxial stress state. Traditionally, the material response to a biaxial stress state has been predicted using theoretical formulations, which utilize the material's mechanical properties measured under uniaxial loading conditions (i.e., yield strength, work hardening exponent, etc.) [4–6]. A more accurate prediction of the material response necessitates careful measurements under biaxial loading, followed by the validation and/or calibration of the above theoretical formulations and/or mechanical properties. Here, a biaxial loading and measurement system requires [1] that: (1) The specimen probe area is within a well-defined biaxial state of stress, (2) The loading apparatus must be capable of providing a large deformation to the specimen, and (3) The system should account for anisotropic material properties.

In industrial practice, a standard method used to determine the failure criterion for sheet metals is based on the construction of the forming limit diagram using the Nakajima bulge

Extended author information available on the last page of the article

test [7]. This methodology was further improved with digital image correlation (DIC) to measure the strain distribution on the sheet providing experimental data to validate the theoretical mechanics formulations. Another common type of testing methodology uses a loading apparatus with multiple load cells to test specimens with a cruciform geometry [1, 8–10]. In this test, planar biaxial stress states with varying biaxiality ratio can be applied to investigate the material behavior along different loading paths [9].

While the aforementioned testing methodologies provide useful guidelines for metal forming operations and help inform theoretical mechanics of response to biaxial loading at the mm level, they can only provide limited information on the elastic and plastic behavior at the micron level through post-mortem *microstructural* analysis. Additionally, these methodologies ignore the effect of the material anisotropy in the biaxial response.

This scope for improvement has been realized recently through *in-situ* measurements during biaxial loading with lab X-ray [11], neutron [12, 13] and synchrotron [14, 15] sources. While other *in-situ* sample geometries (such as sheet [11] and cylinder [16]) have been employed to probe materials using these techniques, the cruciform has been the sample geometry of choice in various experimental setups for *in-situ* diffraction experiments during biaxial loading [12–15, 17]. While these setups allow the cruciform sample to be subject to different biaxial strain ratios and complex strain paths, they are limited by thin sample sizes and need for non-standard sample geometry optimization [12]. The measured elastic strain response to the applied biaxial loading has provided critical information to incorporate and validate crystal plasticity models [13, 17, 18]. Additionally, these methodologies have been leveraged to understand the quantitative evolution of dislocation density/crystallite size (via peak broadening) and a qualitative evolution of texture (via peak intensity) during biaxial loading conditions under varying degrees of biaxiality [19]. *In-situ* lab X-ray studies at NIST have probed diffraction elastic constants [11, 20] and elastic lattice strain response to applied biaxial loading [11, 17]. Using *ex-situ* full texture measurements (from neutron diffraction at various biaxial loads) and visco-plastic self-consistent (VPSC) simulations, these studies have extended the experimental findings from x-ray studies to produce flow curves of the material under biaxial loading.

The apparatus presented in this article mimics the Nakajima bulge test and uses oil pressure to generate the biaxial loading similar to the hydraulic system used to test for biaxial flexure reliability of ceramics in [21]. The apparatus is distinct from the ones used in studies outlined previously in the following ways: (1) Samples closer to actual sheet thickness (~ 1 mm) can be measured which is an improvement over cruciform samples whose probe area thickness is less than 0.5 mm; (2) The applied biaxial strain ratio is fixed for

a given applied oil pressure and only depends on the location from the center. The key advantages of the oil-pressure based apparatus are: (1) It is relatively easy for design/operation and low-cost compared to the cruciform sample setups, (2) A significantly large area (~ 10×10 mm^2) on the sample is accessible for measurement, which allows for a spatially resolved acquisition of the mechanical response of highly heterogeneous and/or anisotropic microstructures.

Due to their economical nature (low alloy content) and attractive mechanical properties, advanced high-strength steels (AHSS) are considered as promising candidates for automotive parts. The unique processing routes enable the formation of different amounts of soft (ferrite, austenite, bainite) and hard (martensite) [22] in the microstructure with a good combination of strength and formability. A recent addition to this new generation of steels is the "flash-processed steel" [23], which is the material of interest in this work. Developed by Cola et al. [23–26], flash processing (FP) involves rapid heating of the steel sheet to the austenitic temperature range followed by quenching to room temperature. The time-temperature combinations in the FP method do not allow for either complete dissolution of carbides or the redistribution of carbon within the austenite, and result in complex mixed microstructure. This mixed microstructure [27–30], distributed homogenously along the sheet plane and through its thickness facilitate good formability during metal forming, while the finished parts maintain a high specific strength during service. The mixed microstructure in an FP steel makes it an ideal candidate for the biaxial apparatus designed in the current study as the apparatus allows for a significantly large mapping area and micro-scale determination of mechanical response.

The goals of this work are as follows – (1) Develop, design, and construct an oil-pressure based biaxial test system that can be used inside the synchrotron beamline facility, (2) Confirm the existence of an equi-biaxial stress state at the center of the test sheet in the current apparatus independently using finite element analysis (FEA) and X-ray diffraction measurements, (3) Conduct a proof-of-concept experiment which measures diffraction information as a function of applied biaxial load and location on an FP steel sheet. The sequence of items presented in this article follows the goals of the research work described above.

Materials and Methods

Components of the Biaxial Testing Apparatus

Figure 1 shows a schematic of the biaxial testing apparatus at a beamline for *in-situ* X-ray diffraction data acquisition. The coordinate axes containing the salient directions

corresponding to the sheet being tested will be used throughout the article, i.e., RD – rolling direction, TD – transverse direction and ND – normal direction. A photograph of the biaxial apparatus before assembly and after assembly can be seen in Fig. 2(a) and (b), respectively. The metal sheet (Fig. 2(a) – (5)) to be tested is clamped onto the sheet stage holder (Fig. 2(a) – (3)) using a sheet stage clamp (Fig. 2(a) – (2)). The hand pump (Fig. 2(b) – (7)) is used to pump the oil from the reservoir through the oil inlet (Fig. 2(a) – (4)) to apply pressure on the test sheet. The oil pressure is monitored using a digital pressure gauge (Fig. 2(a) – (1)),

with a safety valve (Fig. 2(a) – (6)) as a hazard control. A photograph of a test sheet after biaxial testing is shown in Fig. 2(c). Figure 2(d) shows an enlarged view of the location where the bulging occurred.

Beamline Setup for *In-Situ* Experiments Using the Biaxial Testing Apparatus

A photograph of the placement of the biaxial testing apparatus in the beamline, taken from the incident beam side (i.e., looking downstream), is presented in Fig. 3(a). Experiments in the current study were performed in the high-energy synchrotron X-ray beamline 1-ID-E at the Advanced Photon Source (APS), Argonne National Laboratory. Monochromatic X-rays, with a wavelength of 0.173 Å (E=71.676 keV) and a beam size of 150 μm × 150 μm, impinge on the sample through the circular window (Fig. 3(a) – (1)) present on the upstream side of the sheet stage holder. The Debye-Scherrer diffraction patterns (Fig. 1) from the family of crystallographic planes satisfying the diffraction condition are captured by an area detector (GE_41RT) placed downstream of the biaxial apparatus and the steel sheet sample (Fig. 3(a) – (3)). Further, a photograph from the detector side (i.e., looking upstream) of the biaxial apparatus is shown in Fig. 3(b), with a red square marking the nominal area where X-ray measurements were performed and a green dashed circle marking the area subjected to biaxial loading. A schematic of the 9×9 measurement grid used in the current study is shown in Fig. 3(c) within the green dashed circle. The step size (both in the vertical and horizontal directions) between two grid points is 0.5 mm and the exposure time per point is 0.3 s.

The *in-situ* measurements were conducted as the applied oil pressure is systematically changed in steps of 100 psi from 0 to 1000 psi (except at 600 psi, as measurements were
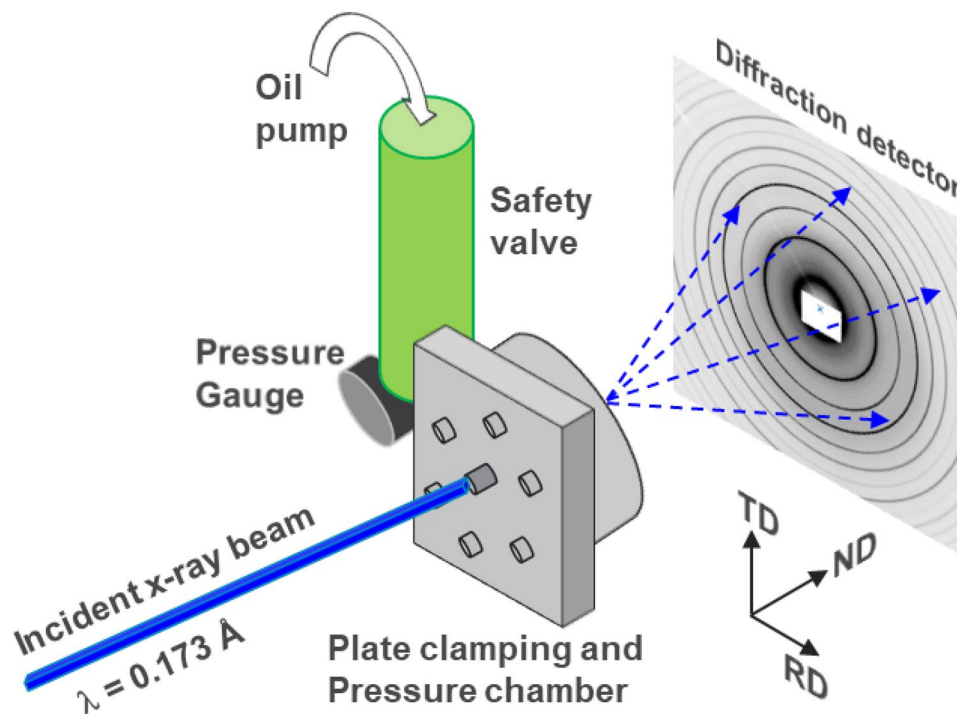

Fig. 1 A schematic of the biaxial testing instrumentation working with *in-situ* X-ray diffraction data acquisition in transmission mode. The metal sheet to be tested is clamped onto a rectangular slab using a cylindrical clamp. The pressure-generating oil is passed through the rectangular slab and maintained/monitored through the hand pump and pressure gauge. Simultaneously, a monochromatic X-ray beam impinges on the sample, through the circular window in the rectangular slab, interacts with the pressurized sheet. The resulting Debye-Scherrer diffraction patterns (e.g., pattern obtained for 0 MPa at center location 41 is shown) are recorded on an area detector. The incident X-ray beam is shown as a solid blue line and the diffracted rays are shown in dotted blue lines. Note that the salient directions corresponding to the tested sheet (TD, RD, ND) have been shown and will be used as coordinate axes throughout this article. The dimensions and distances presented in the schematic are not to scale

Fig. 2 Photographs of the biaxial testing apparatus – (**a**) before assembly, (**b**) after assembly. The components numbered are – (1) Digital pressure gauge, (2) Sheet stage clamp, (3) Sheet stage holder, (4) Oil inlet, (5) Sample test sheet, (6) Safety valve, and (7) Oil pump. (**c**) Photograph of a flash-processed steel test sheet after biaxial testing. (**d**) Enlarged view of the bulge formed after testing with yellow arrows pointing to its circumference. Note that only the region in the yellow dotted rectangle in (**c**) is shown in (**d**). Coordinate axes corresponding to salient sheet directions (TD, ND, RD) are superimposed on the photograph for reference
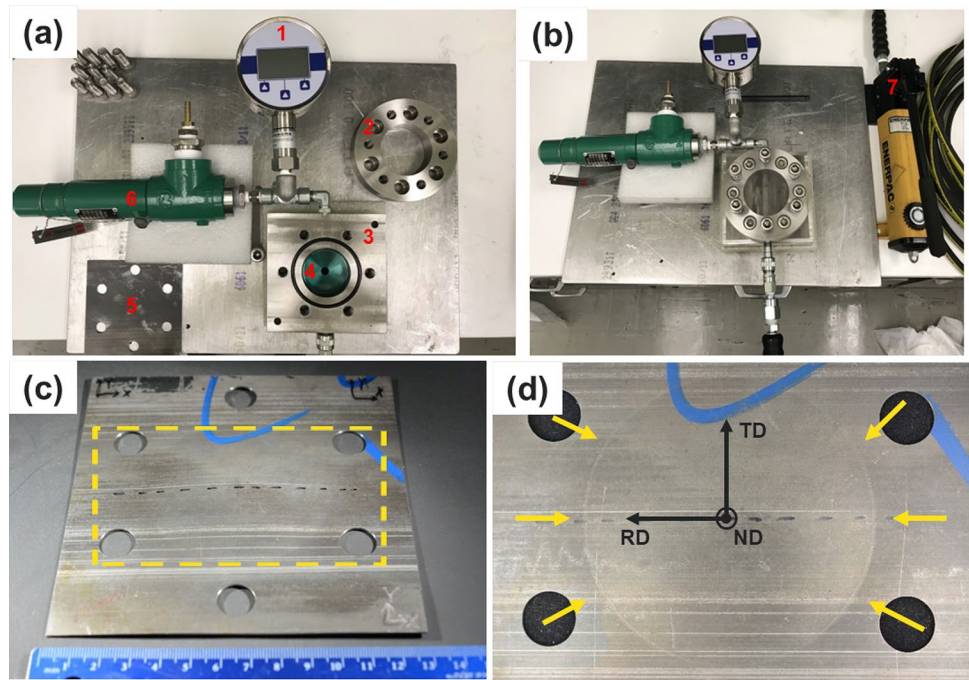
not taken at this oil pressure) and, in steps of 200 psi from 1000 to 2000 psi. Further mention of pressure in the article will use MPa units (note 1 psi = 0.00689 MPa and the converted values have been rounded to three significant figures). At each oil pressure value, Debye-Scherrer diffraction patterns (e.g., Fig. 1) were acquired for each location in the
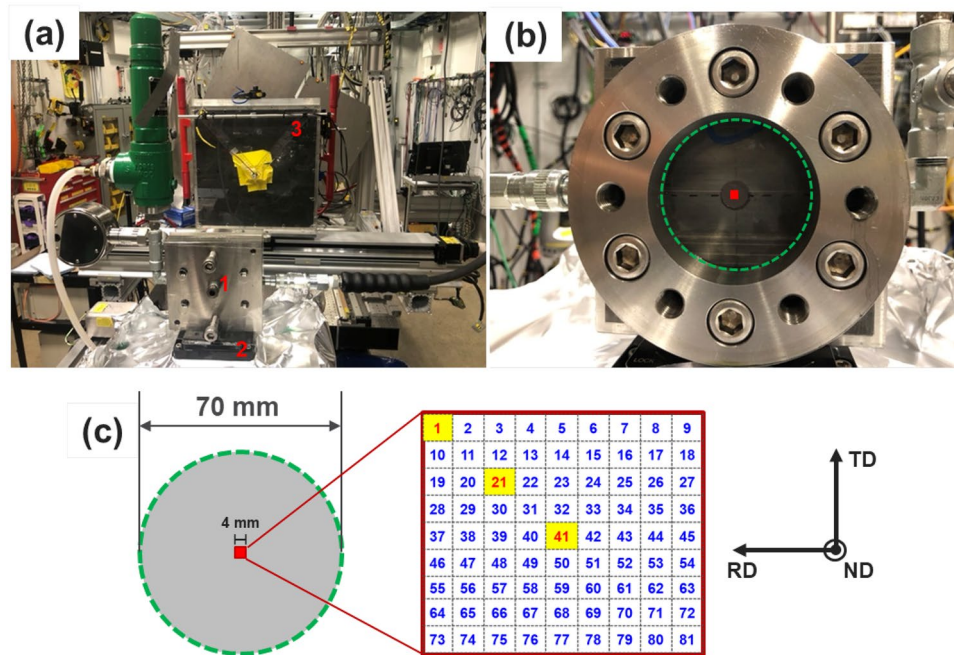

Fig. 3 Photographs of the *in-situ* biaxial testing apparatus within beamline 1-ID-E, APS – (**a**) view from the incident beam side (i.e., looking downstream), (**b**) enlarged view of the cylindrical clamp from the detector side (i.e., looking upstream). The components numbered are – (1) Circular window for incident beam entry, (2) Stage for motion in the RD-TD plane, and (3) Area detector for diffraction data acquisition. The area mapped in the current experiment is shown in the red square and the area subject to the oil pressure is marked using a green dashed circle in (**b**). The red square is enlarged and roughly to scale in (**c**), and a schematic of the rectangular grid of mapping points measured during the current experiment is shown with an enlarged view of the numbering system. Three key locations (1, 21, and 41) used to discuss representative trends later in the article are highlighted. Coordinate axes corresponding to salient sheet directions (TD, ND, RD) are also shown for reference

measurement grid shown in Fig. 3(c). The initial test-sheet-to-detector distance was nominally at 870 mm at 0 MPa. The applied pressure bulges the sample sheet outward towards the detector, changing the sample-to-detector distance (D_{sam}) at each load step and for each measurement point. A gel with a silicon (Si) powder standard (NIST SRM 640c) was applied on the downstream side of the test sheet to allow for recalibration of D_{sam} at each applied oil pressure and for each measurement point.

Workflow for the Analysis of Diffraction Data

The 2-D Debye-Scherrer diffraction rings acquired as a function of applied oil pressure and location were analyzed using GSAS-II [31]. The initial instrument geometry (D_{sam}, detector tilt and beam center) was calibrated using the Si diffraction rings obtained at 0 MPa for one measurement location. Subsequently, using the 0 MPa calibration parameters as the initial value, only D_{sam} was recalibrated at subsequent oil pressures and each measurement point using the Si rings obtained at corresponding pressures and measurement points. The D_{sam} (i.e., distance between the bulge's outer surface and x-ray area detector) obtained for each oil pressure is shown in Fig. 4(a) for three locations on the sample sheet. The detector distance is observed to decrease with increasing oil pressure for all three locations, consistent with the experimental geometry. This can be used to calculate the height of the bulge ($= D_{sam,\ 0\ MPa} - D_{sam,\ x\ MPa}$) as a function of oil pressure as shown in Fig. 4(b). Moreover, Fig. 4(c) and (d) present the D_{sam} extracted for the entire measurement grid at 1.38 MPa and 13.8 MPa, respectively. While the values of the D_{sam} are different, it appears that their variation in the measurement area is similar for both the oil pressures. This observation implies that the calibrant silicon gel in the measured area does not bulge enough in itself to cause significant variation in elastic lattice strain as a function of location on the measurement grid. Further, the uneven spread of detector distances observed in the measurement grid likely arises as an artefact from the diffraction setup and/or a due to a slight unevenness in the thickness of the silicon gel after application. This uneven spread as a function of location on the measurement grid is already accounted for in the D_{sam} obtained after recalibration. The D_{sam} obtained after recalibration procedure at each oil pressure and measurement location provides helps separate out the apparent increase in elastic lattice strain caused by the peak position shift due to sample bulging (i.e., decrease in detector distance) as presented in Fig. 5(b).

Further - sector integrations (also called "caking" or "radial-azimuthal sectoral binning") of 10° at TD and RD ($\pm 5°$ on each side) were performed to obtain 1-D diffraction patterns for each location at each pressure value (Fig. 5(a)). These 1-D diffraction patterns were analyzed using the single peak fitting routine in GSAS-II to extract the positions of the salient peaks in the diffraction pattern of the test sheet. Each peak was fit using a Gaussian peak shape. The step-by-step recipes followed for both the calibration/recalibration at each oil pressure and subsequent single peak fit analysis in GSAS-II package are detailed in the Appendix section of the article. A MATLAB routine scripted in-house was used to extract and present the relevant values from the large.csv files obtained at the end of sequential peak fitting.

Sample Processing and Basic Microstructural Details for the Test Sheets

The test sheets used were 1.02 mm thick 1020 steel (a low carbon steel) sheets subject to 1125 °C flash-processing at Flash Steel Works, MI, USA. Previous microstructural studies on steels processed using FP [27, 29] show the presence of a combination of α-BCC (body-centered cubic) ferrite and/or BCT (body-centered tetragonal) martensite/bainite matrix with orthorhombic Fe_3C precipitates. In this study, the major matrix phase was taken to be α-BCC (Fig. 5(a)). Although most of the minor peaks correspond to silicon standard (marked using blue squares in Fig. 5(a)), the broad unidentified peaks (marked using black triangles in Fig. 5(a)) could correspond to the carbides and nitrides expected to be seen in the microstructure.

Evidence of Equi-biaxial Stress at the Measured Area

Structural Analysis

Finite element analysis of a sheet (also referred to as "plate" in this section) subject to biaxial loading using the test system was performed to determine a correlation between applied oil pressure and stress state at various locations on the steel sheet. The analysis was performed utilizing the tensor mechanics modules of Multiphysics Object Oriented Simulation Environment (MOOSE) [32], an open source finite element code developed by Idaho National Lab, USA. The simulated test sheet was composed of a low-alloy 4130 steel with a thickness of 1.02 mm and diameter of 69.85 mm – following the geometry of the experimental test setup. The deformation was modeled as elastic-plastic with isotropic hardening following the tensile test data from [33] measured for flash processed 4130 steel (a medium carbon steel). The elastic modulus and Poisson's ratio used were 205 GPa and 0.29, respectively [33].

Figure 6(a) illustrates a quarter of the simulated sheet with the applied displacement boundary conditions and the finite element mesh used in the model, along with the coordinate system and salient locations on the simulated sheet. The finite element mesh was chosen through a mesh sensitivity study wherein the initial simulation was performed
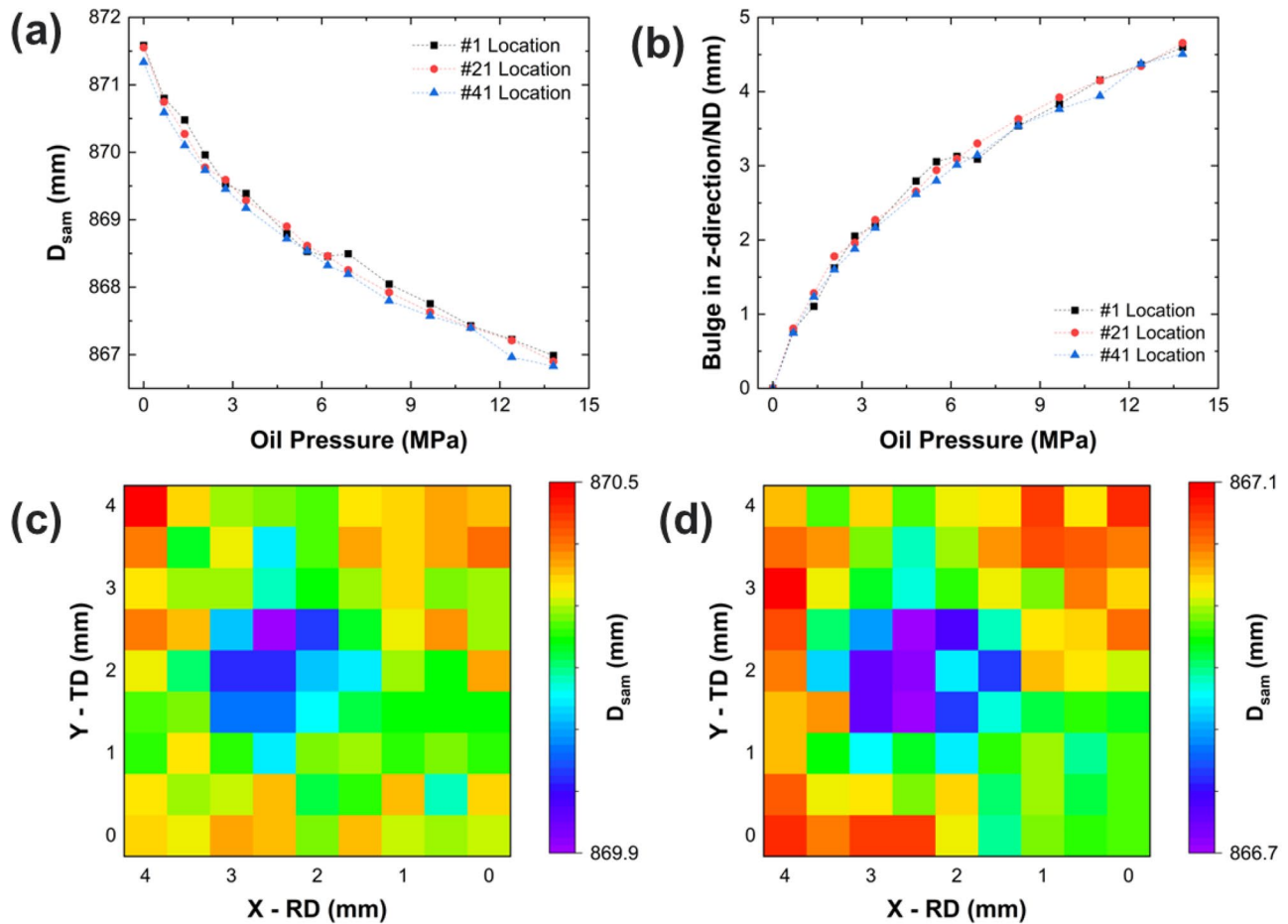
Fig. 4 (**a**) The change in distance of the bulge's outer surface (D_{sam}) from the x-ray area detector for – extracted through recalibration using Si Debye rings at each oil pressure. The inset highlights the three locations (refer Fig. 3(c)) on the measurement grid for which the detector distance (D_{sam}) variations are presented. (**b**) The height of the bulge on the sample sheet as a function of applied oil pressure extracted from the x-ray method. The D_{sam} obtained after recalibration as a function of location on the measurement grid for (**c**) 1.38 MPa, and (**d**) 13.8 MPa

using a coarse mesh followed by simulations with progressively refined meshes until the through-thickness stress values converged, as depicted in Fig. 7(a). Figure 5(b–d) show the distribution of the normal stress components in the x, y and z directions (i.e. σ_{xx}, σ_{yy}, σ_{zz}) in the sheet under an oil pressure of 6.89 MPa applied to the bottom surface of the sheet. Note that the x, y, and z co-ordinates correspond to -RD, TD and ND in real sample coordinates, respectively. The contour plots qualitatively show that values of σ_{xx} and σ_{yy} are very close to each other but distinctively different from σ_{zz} at the center of the sheet. This qualitative observation is quantitatively supplemented by Fig. 7(b). Furthermore, the radial variation of the stress components from the center of the plate is graphically shown in Appendix A2.

All the normal and shear stress components at the center of the sheet from bottom to top at an oil pressure of 6.89 MPa are plotted in Fig. 7(b). These quantitative results show a close match between σ_{xx} and σ_{yy}, while all the other stress components are very close to zero, confirming the

equi-biaxial nature of the stress distribution at the center of the sheet throughout the thickness direction.

Figure 8(a) depicts the stress components at the top-center (i.e., detector-facing/outer surface) and bottom-center (i.e., oil-facing/inner surface) of the sheet as a function of applied oil pressure. The sheet is consistently in a tensile equi-biaxial stress state at the top-center, while the stress state at the bottom-center transitions from compressive equi-biaxial for at lower oil pressures to tensile equi-biaxial at higher oil pressure.

The shift from increasing compressive to increasing tensile stress at the bottom can be attributed to the material's deformation behavior switching from elastic to plastic. Under low applied pressure, the sheet follows linear elastic beam bending, exhibiting tensile stress on the top surface and compressive stress on the bottom surface. However, as the applied pressure increases and plastic deformation is initiated in the material, both the top and bottom center of the sheet eventually experience a tensile stress state.
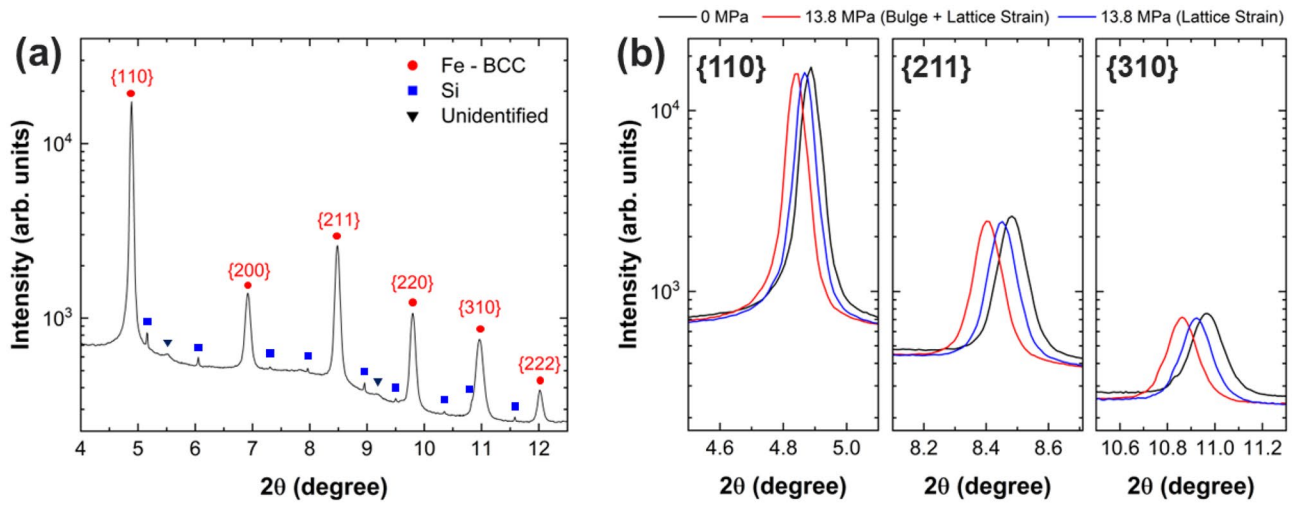
Fig. 5 (**a**) A representative 1-D diffraction pattern obtained after sector integration of 10° along TD at location 41 (center of the grid) at 0 MPa. The major peaks corresponding to FP steel's BCC structure are labeled in red circles (and indexed), along with the minor peaks corresponding to the Si calibrant (blue squares) and broad unidentified peaks (black triangles). (**b**) The peak position shift at 0 MPa (black), at 13.8 MPa without recalibration (red), and at 13.8 MPa after recalibration (blue) shown for three BCC peaks. This highlights the necessity for the recalibration procedure to separate out the contribution of sample bulging to the peak position shift and consequently, the elastic lattice strain

Figure 8(b) shows the evolution of elastic strain component in the x-direction (ε_{xx}) with increasing oil pressure in the simulated sheet. Note that only ε_{xx} is shown, since $\varepsilon_{xx} \sim \varepsilon_{yy}$ for all oil pressures. The ε_{xx} is shown for the top-center and bottom-center locations on the simulated sheet along with their "average", i.e., ($\varepsilon_{xx,\text{top-center}}$ + $\varepsilon_{xx,\text{bottom-center}}$)/2. It is interesting to note that the average ε_{xx} (i.e., through-thickness averaged strain) is consistently positive, inspite of the strain at the bottom-center being

compressive for the initial part of the biaxial loading. Figure 8(c) shows the von Mises effective stress (σ_{VM}) in the bottom-center and top-center of the sheet with increasing oil pressure in the simulated sheet. Given the nominal tensile yield strength of FP 1010 steel (very similar in composition to the 1020 grade used in the current study) was observed to be between 700–800 MPa [28], the material at the sheet center yields at an applied oil pressure of 2 MPa approximately. Further, the material in the top-center and
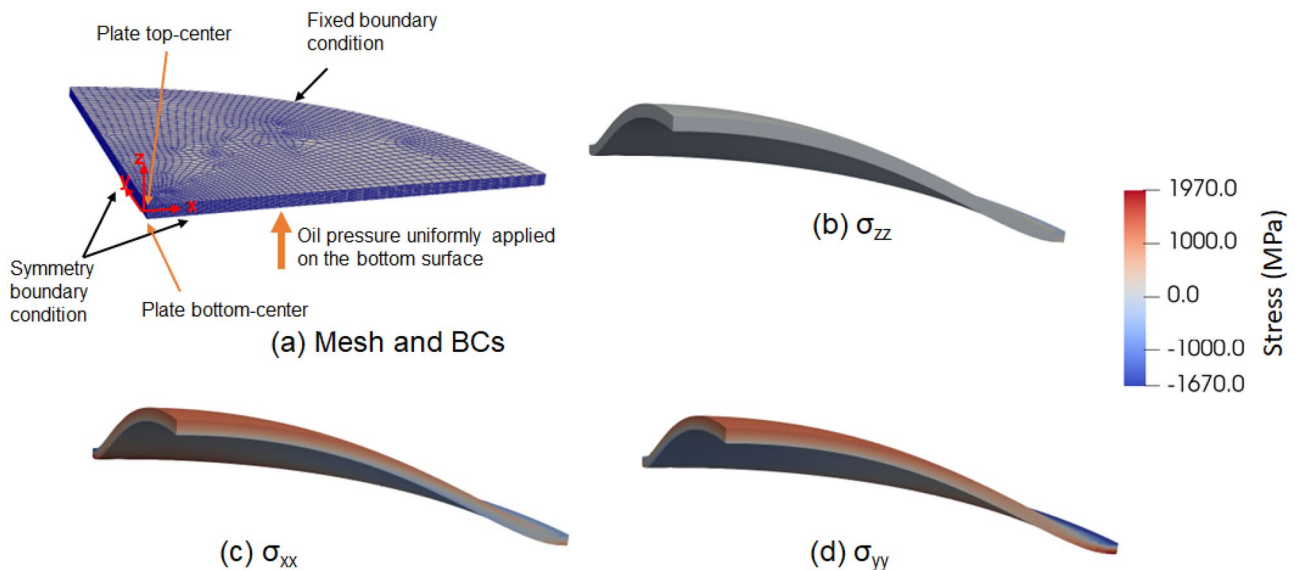

Fig. 6 (**a**) Quarter symmetry finite element model of the sheet with boundary conditions and salient locations marked, (**b–d**) distribution of the normal stress components in the sheet at 6.89 MPa. Deformations are exaggerated fivefold. Note that the x, y, and z co-ordinates correspond to -RD, TD, and ND in real sample coordinates, respectively
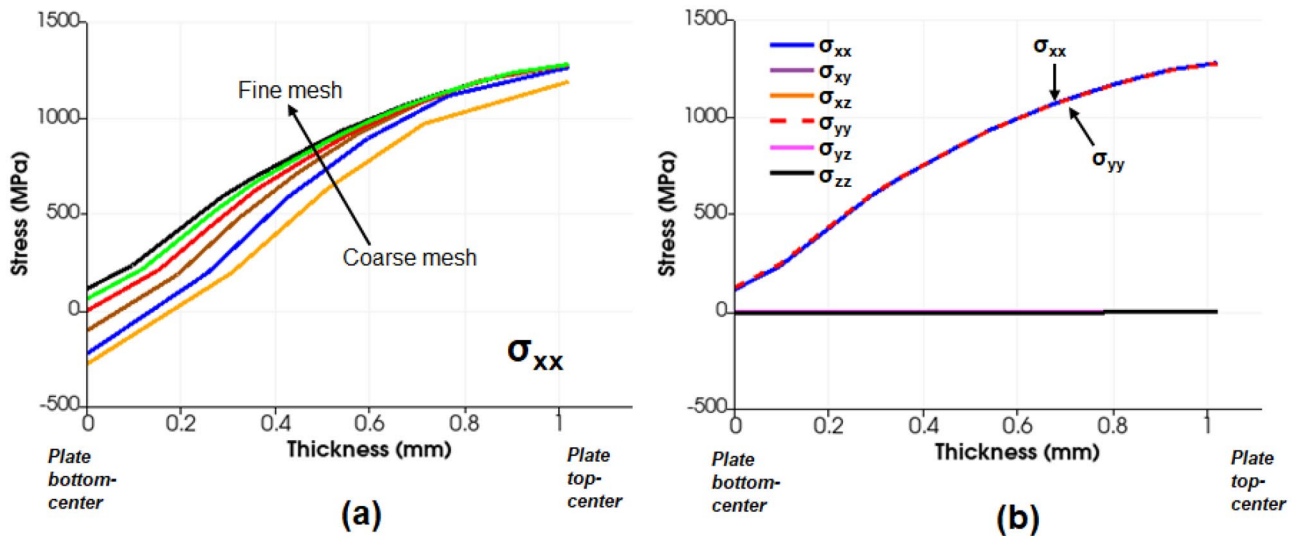
Fig. 7 Through thickness stress distributions at the center of the sheet under the application of 6.89 MPa oil pressure. (**a**) Mesh sensitivity analysis shown for normal stress σ_{xx}, (**b**) Stress components calculated using the optimized fine mesh

bottom-center of the sheet show significant differences in σ_{VM} and thus a corresponding stress gradient through thickness with respect to applied oil pressure.

X-ray Diffraction

In the case of uniaxial tension, the diffraction rings shrink in the loading direction and expand in the perpendicular direction due to the Poisson contraction of the sample in the perpendicular direction [15]. Whereas, in the case of equi-biaxial loading, the rings should ideally expand/contract (depending on the diffraction geometry) with changing load and result in a similar variation of d-spacing as a function of the azimuthal angle for any value of equi-biaxial load [15]. To understand the change in ring position as a function of applied oil pressure, the Debye-Scherrer ring patterns for the 0 MPa and 13.8 MPa (at location 41 in Fig. 3(c)) were caked in sectors of 1° along the azimuth of the patterns from 0 to 360° (RD = 0° and TD = 90°). Note that a 1° sector integration is only used for Fig. 9, however the results in all other figures use a 10° sector integration as described in "Workflow for the Analysis of Diffraction Data" section. This operation yielded a total of 360 1-D diffraction patterns for each oil pressure. A schematic of the sectors is shown in Fig. 9(a). The position of the BCC {110} peak/ring was then extracted using a single-peak fit routine in GSAS-II using the 1-D diffraction patterns obtained from the above operation. Figure 9(b–d) show the variation of the BCC {110} peak position as a function of azimuth angle (from 0 to 360° with RD = 0° and TD = 90°) for 0 MPa and 13.8 MPa – for locations 41, 1, and 21, respectively. The {110} peak position variation as a function of the azimuthal angle for both

0 MPa and 13.8 MPa corresponding to each location are nearly identical. This observation indicates that the loading results in the uniform contraction of the Debye rings and consequently implies that the loading condition is indeed equi-biaxial within the measured area. This observation provides an additional proof for the equi-biaxial nature of the stress state at the center of the test sheet, independent of the FEA results which also suggest the same. Furthermore, the uniform contraction of the rings implies the through-thickness averaged strain is always positive, which is in line with the average ε_{xx} trends from the simulated sheet shown in Fig. 8(b).

It is important to note that Fig. 9(b–d) indicate that the ring radius (i.e., {110} peak position) is slightly different between the RD and TD (corresponding to an elastic strain difference ~ 500 µε). This observation might be a result of the difference in residual stress between two directions remanent from one of the material processing operations. Therefore, TD and RD directions were separately caked and interpreted to avoid an averaging effect that might be caused by full integration along the entire azimuth (i.e., 0 to 360° sector integration).

Key Results Extracted From the Diffraction Data

Elastic Strain for a Single Location as a Function of Oil Pressure

The peak positions extracted using single peak fitting analysis on 1-D diffraction patterns, as described in "Workflow for the Analysis of Diffraction Data" section, were used to
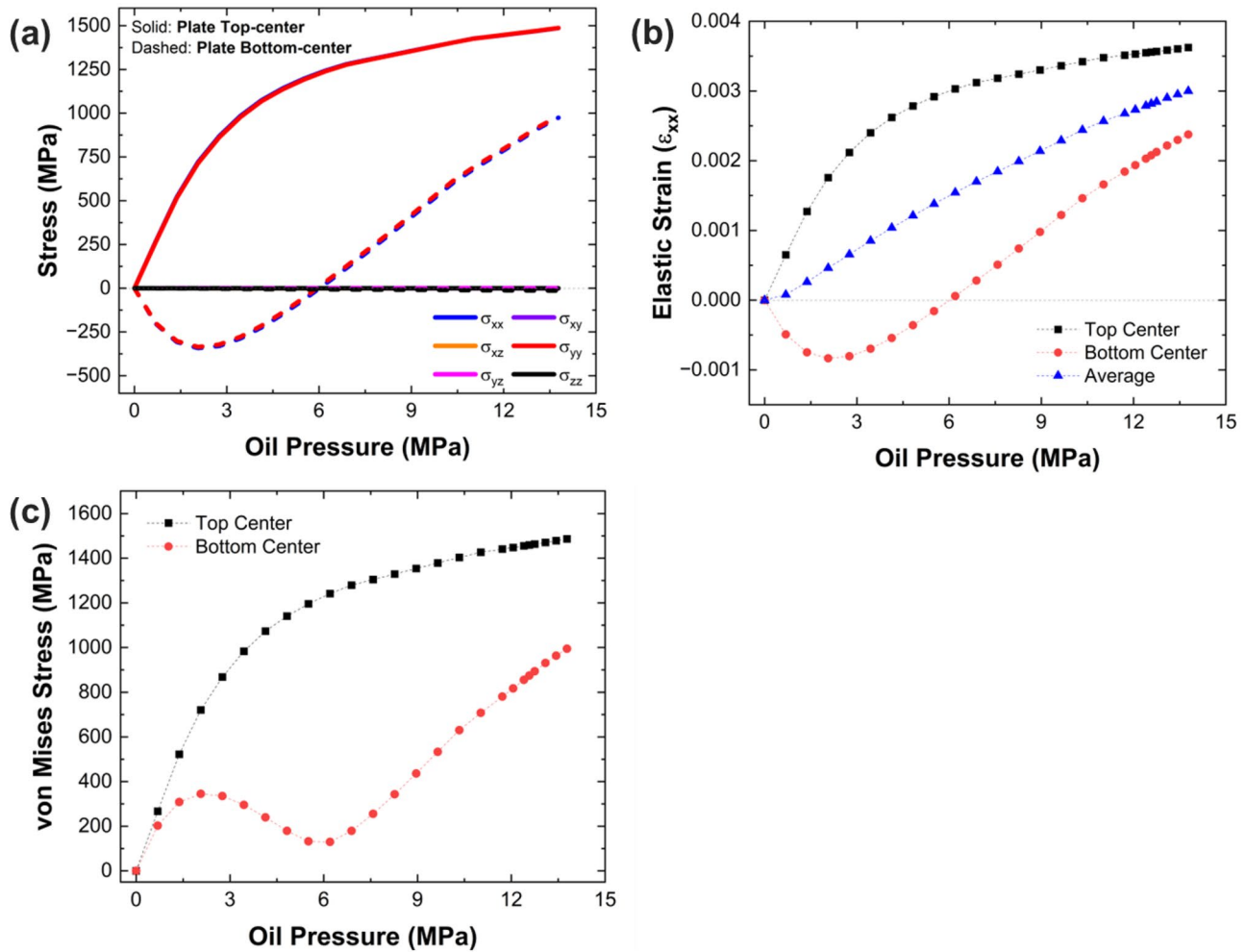
Fig. 8 (**a**) Stress vs oil pressure at the top-center and bottom-center of the simulated sheet, (**b**) Elastic strain (ε_{xx}) as a function of oil pressure at the top-center, bottom-center, and their average, (**c**) von Mises effective stress at the top-center and bottom-center of the simulated sheet

calculate elastic strain for each of the 6 BCC {hkl} peaks using the following equations:

$$\lambda = 2d_{hkl} \sin \theta_{hkl} \quad (1)$$

$$\varepsilon_{hkl} = \frac{d_{hkl} - d_{hkl,0}}{d_{hkl,0}} \quad (2)$$

where, λ is the X-ray wavelength (Å), θ_{hkl} is the Bragg angle (°) for a given {hkl}, d_{hkl} is the interplanar spacing (Å) for a given {hkl}, $d_{hkl,0}$ is the interplanar spacing for a given {hkl} at 0 MPa, and ε_{hkl} is the elastic strain for a given {hkl}. For the results shown in "Elastic Strain for a Single Location As a Function of Oil Pressure" and "Elastic Strain Maps As a Function of Pressure" sections, the sector integration angle used was 10° (i.e., ±5°) about two perpendicular directions – RD (from 355° to 5°) and TD (from 85° to 95°). Note that the elastic strain at any applied oil pressure is with reference to or relative to the 0 MPa measurement. The common

practice is to calculate elastic strain using the measurement of the strain-free interplanar spacings (d_0) from an annealed sample. However, since an annealing operation might destroy the unique mixed microstructure in the FP steel, we resorted to comparative analyses relative to the interplanar spacings from the 0 MPa measurement. Furthermore, the elastic strains obtained here are averaged over the sheet thickness as the diffraction measurement is performed in a transmission geometry.

The elastic strain in six BCC {hkl} families of planes – {110}, {200}, {211}, {220}, {310}, {222} – as a function of applied oil pressure for grid locations 1, 21, and 41 about the TD is presented in Fig. 10(a–c), respectively. Corresponding plots for the RD are shown in Fig. 10(d–f). The elastic strain discussed here is obtained after the recalibration procedure at each oil pressure which separates out the apparent increase in elastic strain, as shown in Fig. 5(b), caused by the contribution of sample bulging to peak position shift. The propagated error in strain
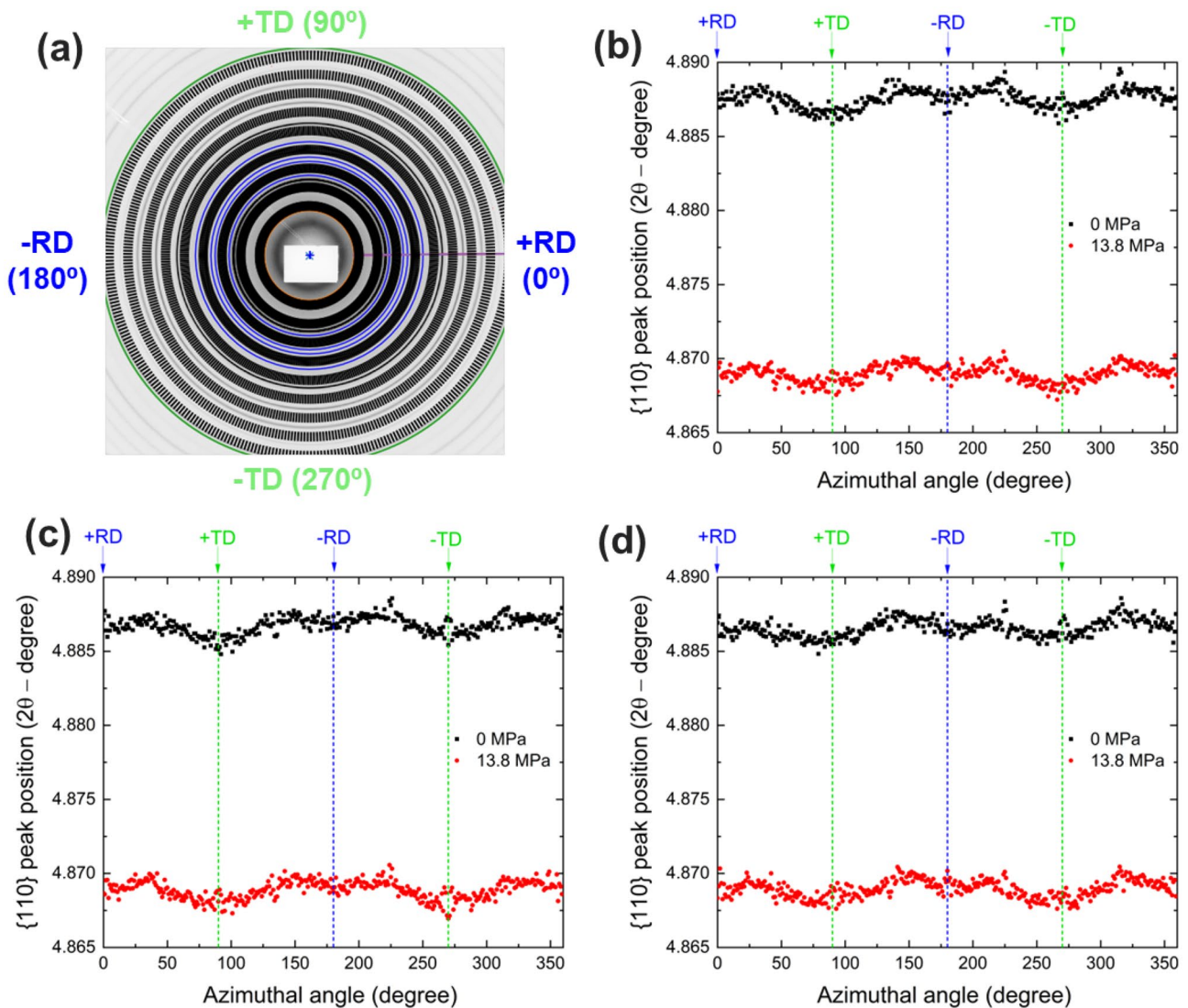
Fig. 9 (**a**) A schematic showing the multiple 1° sector integrations performed along the azimuth of a 2-D Debye-Scherrer pattern to obtain 360 1-D diffraction patterns. The white rectangle at the center of the pattern is the beam stop and the blue "x" mark is the beam center. {110} peak positions, obtained from the 1-D diffraction patterns, plotted as a function of azimuthal angle for 0 and 13.8 MPa for **b** location 41, **c** location 1, and **d** location 21 (refer Fig. 3(c)). ±RD and ±TD locations are marked

calculated from the error in peak position (θ_{hkl}) was smaller than the size of the data markers (i.e., less than ± 50 μɛ) used in Fig. 10. Note that $1 \mu\varepsilon = 1 \times 10^{-6}$ strain units. Diffraction measurements with similar setups have previously been reported [34, 35] to provide a strain resolution of $\pm 1 \times 10^{-4}$ (i.e., ± 100 μɛ). Therefore, the more conservative value of ± 100 μɛ was used as the nominal error bar for strain in the current study.

The elastic strain is observed to follow a qualitatively similar trend - monotonously increasing for all three locations at both RD and TD. In the beginning of the experiment, the measured elastic strains from different {hkl}s remain close to each other. When the oil pressure goes beyond

2 MPa, inducing σ_{VM} to exceed the nominal yield strength of the material, the measured strains from different {hkl}s start to increasingly deviate from each other. The {200} and {310} strains start to take on a larger value compared to the {110} and {222} strains. This difference increases with increasing applied oil pressure. Similar observations have been reported in previous studies on BCC materials under uniaxial and biaxial loading by Collins et al. [15] and Marin et al. [36]. Moreover, the {110} and {220} strains are nearly identical (within error bars), which is consistent with the fact that the crystallographic planes contributing to these strain measurements are nominally identical in the experimental geometry employed in this work.
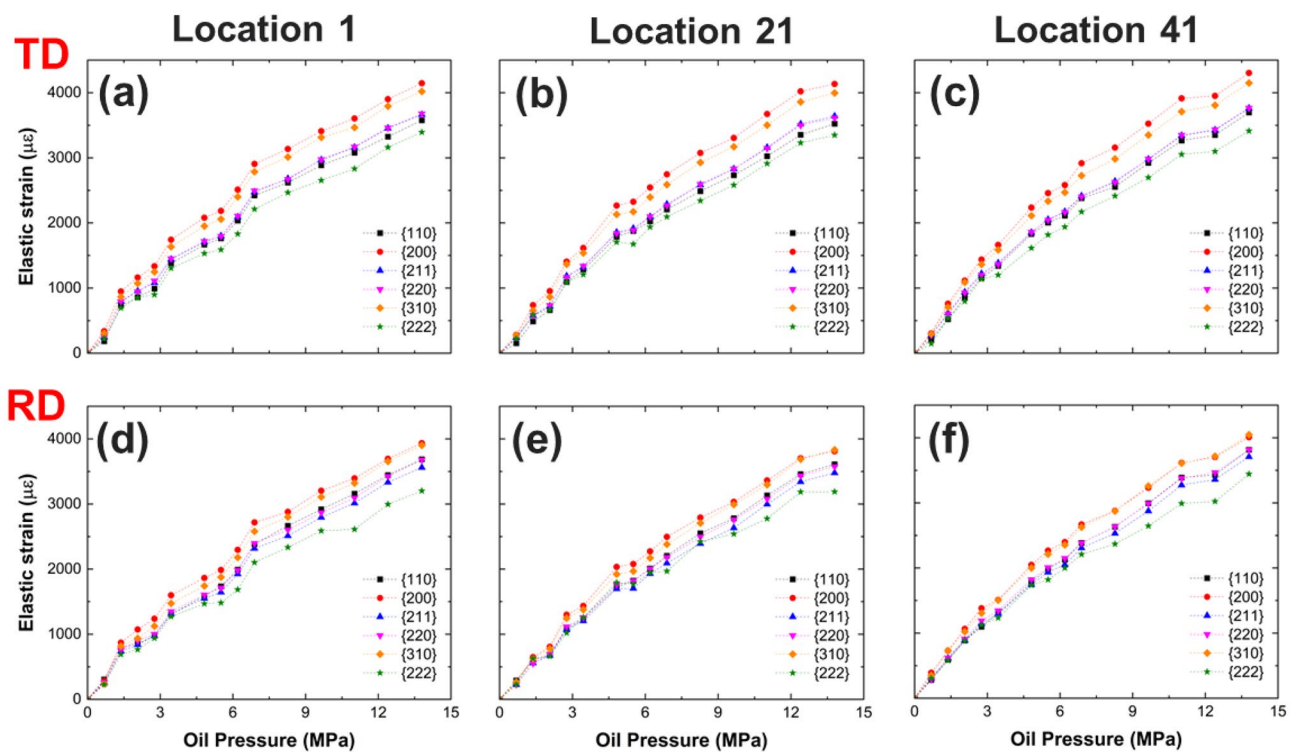
Fig. 10 The evolution of elastic strain (in µε units) in various crystallographic planes for specific locations in the measurement grid as a function of applied oil pressure (in MPa) – (**a**, **b**, **c**) measured along TD, (**d**, **e**, **f**) measured along RD. (**a**, **d**) are measured for location 1, (**b**, **e**) for location 21 and (**c**, **f**) for location 41. Refer Fig. 3(c) for locations on the measurement grid. Note that 1 µε = 1 × 10⁻⁶ strain units

Elastic Strain Maps as a Function of Pressure

Color maps of the spatial variation in {110} TD elastic strain for the entire (9 × 9) measurement grid are shown as a function of applied oil pressure in Fig. 11. As expected, the color maps have been plotted using the same color scale and show a general increase in elastic strain with an increase in the applied oil pressure. The maps change from mostly "purple" colored for 1.38 MPa to mostly "red" colored for 13.8 MPa. Furthermore, within a given colormap (i.e., applied oil pressure) a spread of strain values ≤ 500 µε (appreciably higher than the nominal error bar) is seen. This observation implies that there are relatively hard and soft regions within the microstructure (i.e. different regions in the microstructure accommodate deformation differently) and supports the hypothesis that the unique mixed microstructure is likely one of the key contributors to the improvement in formability of this flash-processed steel [27]. This result also demonstrates a key strength of the current apparatus coupled with a synchrotron x-ray probe – spatially resolved measurement of {hkl}-dependent response to biaxial loading in the meso-scale for heterogenous materials. This information is valuable to the meso-scale deformation modeling community for calibration/validation of their models.

Summary and Future Outlook

The successful design and fabrication of an oil-pressure based biaxial testing apparatus for *in-situ* synchrotron X-ray characterization was detailed, followed by proof-of-concept *in-situ* diffraction experiments on a flash-processed steel sheet. The presence of an equi-biaxial stress state at the center of the test sheet was independently modeled using finite element (FEA) simulations and measured using X-ray diffraction. The measured elastic strains from different {hkl}s were similar at lower oil pressure and start to deviate from each other at higher oil pressures, consistent with anticipated macroscopic yielding. The strain response was clearly different for different locations in the measurement grid supporting the hypothesis that the mixed microstructure in FP steels could play a significant role in enhancing their formability. While the characterization of the through-thickness stress distribution (Fig. 7) was beyond the scope of this work, quantifying this gradient could be technologically interesting as large stress gradients encountered in forming operations could potentially induce location-dependent residual stresses, microstructure, and phase gradients. With advances in novel x-ray instrumentation [34, 37, 38], follow-up studies that exploit the biaxial testing apparatus described here
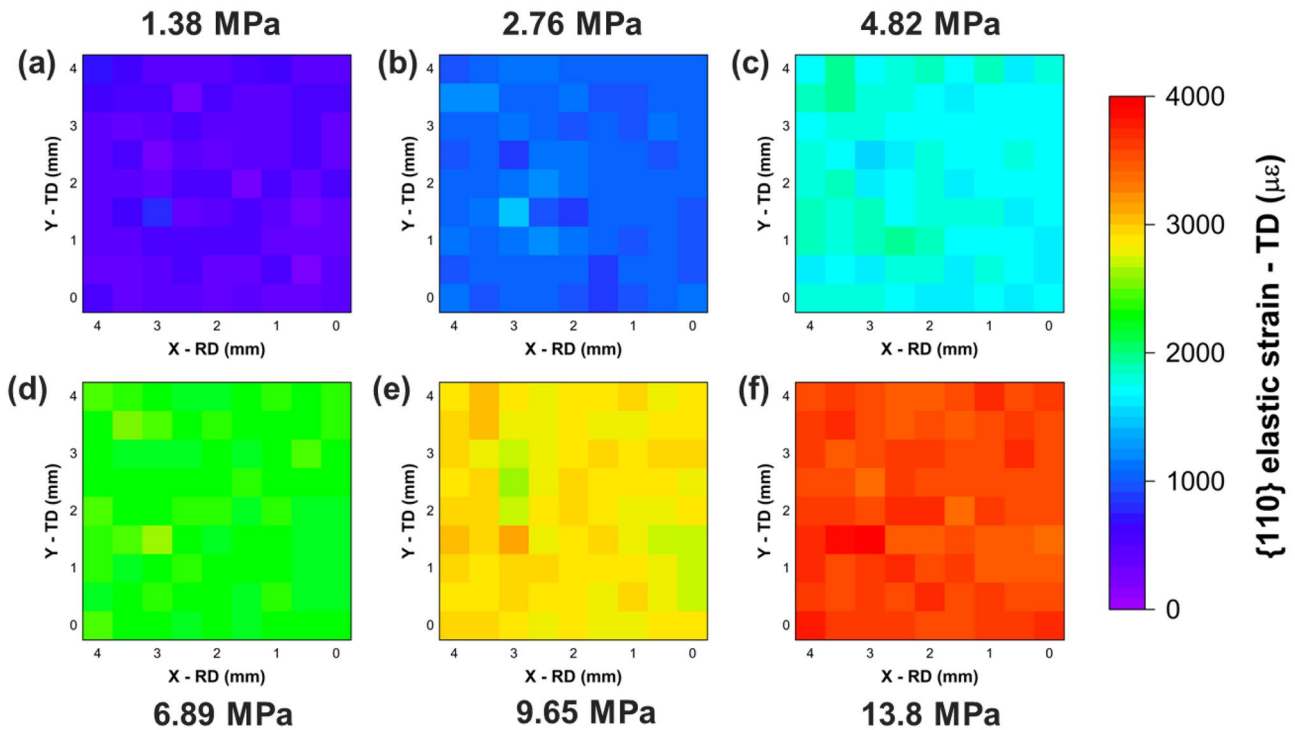
Fig. 11 {110} elastic strain (in TD) color maps for the entire 9×9 measurement grid (in µε units) for a given oil pressure (in MPa) measured along TD – **a** 1.38 MPa, **b** 2.76 MPa, **c** 4.82 MPa, **d** 6.89 MPa, **e** 9.65 MPa, and **f** 13.8 MPa. Note that 1 µε = 1×10^{-6} strain units

to explore the through-thickness stress distributions could be planned.

Moreover, a key improvement achieved in the apparatus fabricated in this work over the current practice of *in-situ* biaxial testing is its relatively easy design/operation and low-cost. Furthermore, this apparatus configuration, coupled with synchrotron x-rays, is an invaluable tool to measure biaxial response of a sheet metal over significant area (~ mm^2) on the sample with a fine resolution (~ 100 m). These capabilities are key to obtain a better fundamental micro-scale understanding of the mechanical response of heterogeneous and/or anisotropic microstructures (such as textured materials or HCP metals/alloys).

Appendix A1 – Step-by-Step Analysis Workflow in GSAS-II

1. **Calibration using Si standard Debye rings**

   (i) Import the diffraction images for the entire 9 X 9 measurement grid for 0 MPa into GSAS-II project using Import > Image > GE Image file

   (ii) Import the rough estimates of calibration parameters obtained using CeO$_2$ using Parms > Load

   Controls > CeO$_2$.imcrtl file (previously saved after calibration using CeO$_2$)

   (iii) Save the GSAS-II project file using Menu > Save project > Direction_Pressure_Sample.gpx

   (iv) Calibrate using the Si rings measured at location 41

   (a) Beam center X, Y, and wavelength are unchanged (i.e., remove tick)

   (b) Inner and outer 2-Theta used were 2.9 and 13.2° to include the first Debye ring corresponding to Si (lower bound) and 7 Debye rings corresponding to steel (upper bound).

   (c) Tick the distance (D$_{sam}$), tilt, and rotation as the parameters to be refined for the calibration process.

   (d) Use Calibration > Calibrate and click on 5 points around the first ring corresponding to Si. Use Calibrate > Recalibrate a few times until the parameters being refined converge to a constant value for the other parameters.

   (e) Untick the tilt and rotation – since further calibration of remaining measurement locations in the grid and all locations at higher pressures will be conducted only for distance (D$_{sam}$).

(f)   Use Parms > Save controls > Si_0MPa.imcrtl to save the calibration parameters obtained at location 41 and use them for higher pressures and the entire measurement grid.

(v)   Calibrate patterns from remaining grid locations at 0 MPa

(a)   Use Parms > Copy controls > Set all (to select all images to calibrate). Make sure distance (D_{sam}) is the only parameter used for calibration.

(b)   Use Calibration > Recalibrate all > Set all to sequentially calibrate the remaining 80 images in the project file. Use Calibrate > Recalibrate all > Set all few times until the distance (D_{sam}) converges to a constant value. In this case, the recalibration was repeated 3 times.

(c)   At the end of this step, each location on the measurement grid (for a given oil pressure) has a unique calibrated distance (D_{sam}).

(vi)   Integrate and use sequential peak fit to obtain the peak position, integrated intensity, and width using the steps described below in Procedure 2.

(vii)   Repeat steps i through vi for the analysis of data from higher pressures in separate project files. Replace step ii with Parms > Load Controls > Si_0MPa.imcrtl file to load the calibration parameters from location 41 of the 0 MPa data instead of the CeO_2 calibration parameters.

2.   **Integration and sequential peak fitting (step vi in the above procedure)**

(i)   Starting with the TD (North direction) - set the integration limits to 85 to 95°. Set radial bins (corresponding to 2-Theta) to a high value (1000 in the present case) and azimuthal bins to 1. Check to make sure the Inner/Outer 2-Theta range is the same as entered in step iv (b) in Procedure 1.

(ii)   Use Integrate > Integrate All > Set all to obtain the sector-integrated 1-D powder patterns corresponding to each location for a given pressure.

(iii)   Use Peak list > Peak fitting > Auto search to start the peak fitting process. Select the peaks corresponding to the material/phase being analyzed and unselect the peaks corresponding to Si and minor phases, if already detected by the Auto Search step. In the present case – the first 6 peaks of the BCC phase were chosen.

(iv)   The Peak list window displays the selected peaks with each of their attributes – peak position, intensity, sigma (Gaussian width) and gamma (Lorentzian width). In the Peak List window, double click on "intensity" and in the pop-up window entitled "Refine" check vary all. Use Peak fitting > Peakfit and repeat this for "position" and "sigma". After all the parameters have been progressively refined as described above, use Peak fitting > Peakfit with all of them selected until they converge (i.e., their values are unchanged after a Peakfit operation). In the present case, gamma is NOT refined.

(v)   Use Peak fitting > Peak copy > Set all to copy the above peaks to all the powder patterns obtained for the images in the given project file. Further, use Peak fitting > Seq. peakfit > Set all to perform a sequential peak fitting operation. The Copy to next feature was enabled (copies the fit values from the current pattern as the initial values for the subsequent pattern) and resulted in a slight decrease in computational time.

(vi)   The sequential peak fit operation results in a table with the residual of fit, peak characteristics and their corresponding error values (standard deviation). Export this table to a .csv file using Seq. export > Save table as .csv. An Rwp (residual) of 10-15% was seen in the present case and indicated a good pattern fit visually.

(vii)   Repeat operations i to vi in Procedure 2 for all pressures to obtain the peak characteristics of multiple peaks for all pressures. To produce results along the RD (East direction), repeat operations i to vi in Procedure 2 with integration limits in step i set between 355° to 5°.

Appendix A2 – Radial Variation of Stress Components from the Plate Center

According to the finite element simulations, shown below in Fig. 12, the stress state at mid-thickness is equi-biaxial near the center of the plate and starts to deviate (>1%, i.e., 12.5 MPa) after a radial distance of about 5 mm from the center. As illustrated previously in Fig. 3c, the measurement grid spanned 4 mm × 4 mm and consequently, the distance between location 1 and 41 is about 2.82 mm. Therefore, all points within the measurement grid were subject to an equi-biaxial stress state.
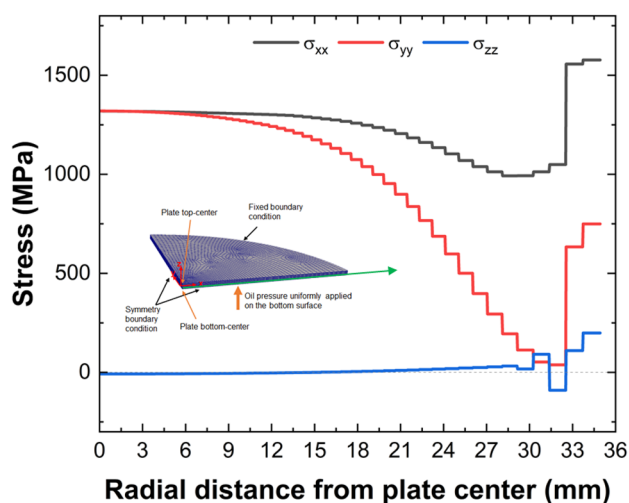
Fig. 12 The variation of stress components at mid-thickness of the plate as a function of radial distance from the center of the plate for an applied oil pressure of 6.89 MPa. The radial direction is marked using a green arrow on the FEA model schematic.

Data Availability Data will be made available by the authors upon reasonable request.

Declarations

Competing Interests The authors declare that they have no known competing financial interests or personal relationships that could have appeared to influence the work reported in this paper.

References

1. Boehler JP, Demmerle S, Koss S (1994) A new direct biaxial testing machine for anisotropic materials. Exp Mech 34:1–9
2. Hannon A, Tiernan P (2008) A review of planar biaxial tensile test systems for sheet metal. J Mater Process Technol 198(1–3):1–13
3. Green DE, Neale KW, MacEwen SR, Makinde A, Perrin R (2004) Experimental investigation of the biaxial behaviour of an aluminum sheet. Int J Plast 20(8–9):1677–1706
4. Zhou M, Clode MP (1997) A constitutive model and its identification for the deformation characterized by dynamic recovery. J Eng Mater Technol 119:138–142
5. Meng B, Wan M, Wu X, Zhou Y, Chang C (2014) Constitutive modeling for high-temperature tensile deformation behavior of pure molybdenum considering strain effects. Int J Refract Metal Hard Mater 45:41–47
6. Xiao R (2019) A Review of Cruciform Biaxial Tensile Testing of Sheet Metals. Exp Tech 43(5):501–520
7. Kuwabara T (2007) Advances in experiments on metal sheets and tubes in support of constitutive modeling and forming simulations. Int J Plast 23(3):385–419
8. Makinde A, Thibodeau L, Neale KW, Lefebvre D (1992) Design of a biaxial extensometer for measuring strains in cruciform specimens. Exp Mech 32(2):132–137
9. Makinde A, Thibodeau L, Neale KW (1992) Development of an apparatus for biaxial testing using cruciform specimens. Exp Mech 32:138–144
10. Kuwabara T, Ikeda S, Kuroda K (1998) Measurement and analysis of differential work hardening in cold-rolled steel sheet under biaxial tension. J Mater Process Technol 80–81:517–523
11. Gnäupel-Herold T, Iadicola M, Creuziger A, Foecke T, Hu L (2013) Interpretation of diffraction data from *In Situ* stress measurements during biaxial sheet metal forming. Mater Sci Forum 768–769:441–448
12. Van Petegem S, Guitton A, Dupraz M, Bollhalder A, Sofinowski K, Upadhyay MV, Van Swygenhoven H (2017) A miniaturized biaxial deformation rig for *in situ* mechanical testing. Exp Mech 57(4):569–580
13. Upadhyay MV, Patra A, Wen W, Panzner T, Van Petegem S, Tomé CN, Lebensohn RA, Van Swygenhoven H (2018) Mechanical response of stainless steel subjected to biaxial load path changes: Cruciform experiments and multi-scale modeling. Int J Plast 108:144–168
14. Hommer GM, Park JS, Brunson ZD, Dahal J, Kenesei P, Mashayekhi A, Almer JD, Vignes J, Lemmer SR, Clausen B, Brown DW, Stebner AP (2019) A planar biaxial experiment platform for In Situ high-energy diffraction studies. Exp Mech 59(5):749–774
15. Collins DM, Mostafavi M, Todd RI, Connolley T, Wilkinson AJ (2015) A synchrotron X-ray diffraction study of *in situ* biaxial deformation. Acta Mater 90:46–58
16. Cakmak E, Choo H, Kang J-Y, Ren Y (2015) Relationships between the phase transformation kinetics, texture evolution, and microstructure development in a 304l stainless steel under biaxial loading conditions: synchrotron X-ray and electron backscatter diffraction studies. Metall and Mater Trans A 46(5):1860–1877
17. Jeong Y, Gnäupel-Herold T, Barlat F, Iadicola M, Creuziger A, Lee M-G (2015) Evaluation of biaxial flow stress based on elasto-viscoplastic self-consistent analysis of X-ray diffraction measurements. Int J Plast 66:103–118
18. Erinosho TO, Collins DM, Wilkinson AJ, Todd RI, Dunne FPE (2016) Assessment of X-ray diffraction and crystal plasticity lattice strain evolutions under biaxial loading. Int J Plast 83:1–18
19. Van Petegem S, Wagner J, Panzner T, Upadhyay MV, Trang TTT, Van Swygenhoven H (2016) *In-situ* neutron diffraction during biaxial deformation. Acta Mater 105:404–416
20. Luzin V, Banovic S, Gnäupel-Herold T, Prask H, Ricker RE (2005) Measurement and calculation of elastic properties in low carbon steel sheet. Mater Sci Forum 495–497:1591–1596
21. Chao LY, Shetty DK (1991) Reliability analysis of structural ceramics subjected to biaxial flexure. J Am Ceram Soc 74(2):333–344
22. Matlock DK, Kang S, De Moor E, Speer JG (2020) Applications of rapid thermal processing to advanced high strength sheet steel developments. Mater Character 166
23. Lolla T, Cola G, Narayanan B, Alexandrov B, Babu SS (2013) Development of rapid heating and cooling (flash processing) process to produce advanced high strength steel microstructures. Mater Sci Technol 27(5):863–875
24. Hanhold B, Babu SS, Cola G (2013) Investigation of heat affected zone softening in armour steels Part 1 – Phase transformation kinetics. Sci Technol Weld Joining 18(3):247–252

25. Hanhold B, Babu SS, Cola G (2013) Investigation of heat affected zone softening in armour steels Part 2 – Mechanical and microstructure heterogeneity. Sci Technol Weld Joining 18(3):253–260

26. Cola Jr GM, Hanhold B, Lolla T, Radhakrishnan B, Babu SS (2013) On the Tensile elongation of advanced high-strength steels. Iron Steel Technol 1–6

27. Shassere B, Babu SS, Cola G, Muth TR, Watkins TR, Control M (2018) Correlation to Formability of Low Alloy Steel Via Flash Processing. Mater Sci Technol (MS&T18), Columbus, Ohio, United States of America 321–328

28. Watkins TR, Cola G, Babu SS, Muth TR, Shassere B, Wang H, Dinwiddie R (2019) Fundamental Science and Technology of Flash Processing Robustness for Advanced High Strength Steels (AHSS), Oak Ridge National Lab. United States. https://doi.org/10.2172/1606795

29. Guo Q, Watkins TR, Trofimov A, Wang H, Cola G, Muth TR, Singh D, Thomas J, Babu S, Unocic KA (2021) Microstructure evolution of low carbon steel via flash processing. Microsc Microanal 27(S1):156–158

30. Radhakrishnan B, Song Y, Gorti S, Cola G (2022) High Performance computing to quantify the evolution of microscopic concentration gradients during flash processing, oak ridge national lab. United States. https://doi.org/10.2172/1885309

31. Toby BH, Von Dreele RB (2013) GSAS-II: the genesis of a modern open-source all purpose crystallography software package. J Appl Crystallogr 46(2):544–549

32. Icenhour C, Keniley S, DeChant C, Permann C, Lindsay A, Martineau R, Curreli D, Shannon S (2018) Multi-physics Object Oriented Simulation Environment (MOOSE), Idaho National Lab. United States. https://www.osti.gov/servlets/purl/1498270

33. Vigilante G, Hespos M, Bartolucci S (2011) Evaluation of flash bainite in 4130 Steel, U.S. Army ARDEC. https://doi.org/10.21236/ada588144

34. Park JS, Chuang AC, Okasinski J, Chen H, Shade P, Turner TJ, Stock S, Almer J (2022) A new residual strain mapping program using energy dispersive X-Ray diffraction at the advanced photon source. Exp Mech 62(8):1363–1379

35. Brown DW, Okuniewski MA, Almer JD, Balogh L, Clausen B, Okasinski JS, Rabin BH (2013) High energy X-ray diffraction measurement of residual stresses in a monolithic aluminum clad uranium–10wt% molybdenum fuel plate assembly. J Nucl Mater 441(1–3):252–261

36. Marin T, Dawson PR, Gharghouri MA, Rogge RB (2008) Diffraction measurements of elastic strains in stainless steel subjected to *in situ* biaxial loading. Acta Mater 56(16):4183–4199

37. Martins R, Lienert U, Margulies L, Pyzalla A (2001) Residual strain tensor determination within highly plastically deformed torsion samples using high energy synchrotron radiation. J Neutron Res 9(2–4):249–254

38. Hou P, Li Y, Zhang W, Chae D, Park J-S, Ren Y, Gao Y, Choo H (2021) Synchrotron x-ray diffraction and crystal plasticity modeling study of martensitic transformation, texture development, and stress partitioning in deep-drawn TRIP steels. Mater 18

Authors and Affiliations

R.R. Kamath[1] · J. Thomas[1] · A.C. Chuang[2] · B. Barua[1] · J.-S. Park[2] · L. Xiong[1] · T.R. Watkins[3] · S.S. Babu[4] · G. Cola[5] · D. Singh[1]

✉ R.R. Kamath
rrkamath@anl.gov

[1] Applied Materials Division, Argonne National Laboratory, Lemont, IL 60439, USA

[2] X-ray Science Division, Argonne National Laboratory, Lemont, IL 60439, USA

[3] Materials Science & Technology Division, Oak Ridge National Laboratory, Oak Ridge, TN 37830, USA

[4] Manufacturing Sciences Division, Oak Ridge National Laboratory, Oak Ridge, TN 37830, USA

[5] Flash Steelworks, Washington, MI 48095, USA